

## ARTICLE OPEN



# Controlling surface porosity of graphene-based printed aerogels

Binghan Zhou<sup>1</sup>, Zhuo Chen<sup>1</sup>, Qian Cheng<sup>2</sup>, Mingfei Xiao<sup>1</sup>, Garam Bae<sup>1</sup>, Dongfang Liang<sup>2</sup> and Tawfique Hasan<sup>1</sup>✉

The surface porosity of graphene-based aerogels strongly influences their performance in applications involving mass transfer. However, the factors determining the surface porosities are not well-understood, hindering their application-specific optimisation. Here, through experiments and hydrodynamic simulations, we show that the high shear stress during the graphene-based aerogel fabrication process via 3D printing leads to a non-porous surface. Conversely, crosslinking of the sheets hinders flake alignment caused by shearing, resulting in a porous surface. Our findings enable fine control of surface porosity of printed graphene-oxide aerogels (GOA) through regulation of the crosslinking agents and shear stress. Using this strategy, we demonstrate the performance advantages of GOA with porous surface over their non-porous counterpart in dye adsorption, underscoring the importance of surface porosity in certain application scenarios.

*npj 2D Materials and Applications* (2022)6:34; <https://doi.org/10.1038/s41699-022-00312-w>

## INTRODUCTION

In the past decade, great efforts have been made to develop graphene-based aerogels due to their unique structural and physical properties<sup>1,2</sup>. Compared to the traditional shaping methods for these aerogels, 3D printing technology stands out due to its ability to create high-precision, complex patterns, and scaffolds without templates.<sup>3</sup> The majority of applications of graphene-based aerogels, such as energy storage<sup>4,5</sup>, gas sensing<sup>6,7</sup>, chemical adsorption<sup>8,9</sup>, and catalysis<sup>10</sup> involve an essential mass transfer process. In these scenarios, the surface porosity of the aerogels is critical to facilitate the flow or diffusion of the reactive materials through their surface<sup>11,12</sup>. Control of surface porosity is therefore crucial to optimise the performance of 3D printed aerogels. The ink properties, which are usually modified through additives in graphene oxide (GO) suspensions and the print parameters are likely to play decisive roles in the surface porosity for graphene-based aerogels. This is because the common post-printing processes such as thermal<sup>13</sup>, chemical<sup>14,15</sup>, or microwave<sup>16</sup> reduction do not significantly alter the surface morphology. Although there has not been any comprehensive experimental evidence, it is widely postulated that the shear flow inside the extrusion nozzle determines the alignment of 2D sheets with respect to the inner walls<sup>13,17–19</sup>.

Indeed, there have been reports on aerogels ranging from non-porous surfaces fully covered with stacked graphene sheets, to the porous surface with radially distributed graphene sheets, without any clear pattern (see Supplementary Table 1). For example, ref. <sup>20</sup> fabricated GOAs with a non-porous surface with parallel stacked graphene sheets using hydroxypropyl methylcellulose (HPMC) as an additive. Using freeze-casting, ref. <sup>15</sup> directly extruded pure GO suspension to print a monolith with a non-porous aerogel surface. On the contrary, there have been reports suggesting GO inks gelled by ascorbic acid (AA)<sup>13</sup>, Ca<sup>2+</sup><sup>14</sup>, sodium alginate<sup>21</sup>, or urea<sup>22</sup> result in aerogels with a porous surface. It has been noted that the level of crosslinking between the GO sheets that are induced by the additives can also affect the surface porosity of the aerogels. Therefore to achieve a degree of control over the surface

structures, a better understanding of the key parameters determining the porosity affecting the above studies is necessary.

Here, we report a systematic investigation of the surface porosity of 3D printed graphene-based aerogels. We demonstrate two critical parameters to quantitatively adjust the surface porosity of these aerogels. Through hydrodynamic simulations and experiments with flow rates, extrusion nozzle and chemical additives, we show that high shear stress during printing directly leads to a non-porous aerogel surface. This is due to the alignment of the sheets with the internal wall of the nozzles. We also show that crosslinking of graphene-oxide sheets offsets the shear stress-induced alignment and contributes to the porosity of the aerogel surface. We additionally demonstrate the importance of surface porosity regulation through difference in dye-adsorption performance between aerogels with porous and non-porous surfaces.

## RESULTS AND DISCUSSION

### Shear stress in printing and surface porosity

To avoid interference from other factors that might affect the surface morphology (such as substrate type or solvent evaporation), aerogel filaments are obtained by direct extrusion into liquid nitrogen (Fig. 1a), followed by freeze-drying. We additionally introduce an optical method to estimate the degree of porosity for quantitative description of surface morphology, as discussed in Methods. For this, we define the surface porosity as the ratio between the pores' area to the total surface area from SEM images of the centre of the filament. As demonstrated in Supplementary Fig. 1a, the surface porosity of a typical filament with a non-porous surface is close to zero. Hence, we define a surface to be non-porous when the surface porosity is smaller than 5%. When the surface porosity falls between 5 to 40%, the aerogel filaments are considered to be semi-porous (Supplementary Fig. 1b). And finally, we consider the surface to be porous for values above 40% (Supplementary Fig. 1c). The adjuncts "porous" and "non-porous" in the following discussion are used to describe the surface of the printed aerogels.

<sup>1</sup>Cambridge Graphene Centre, University of Cambridge, Cambridge CB3 0FA, UK. <sup>2</sup>Department of Engineering, University of Cambridge, Cambridge CB2 1PZ, UK. ✉email: th270@cam.ac.uk

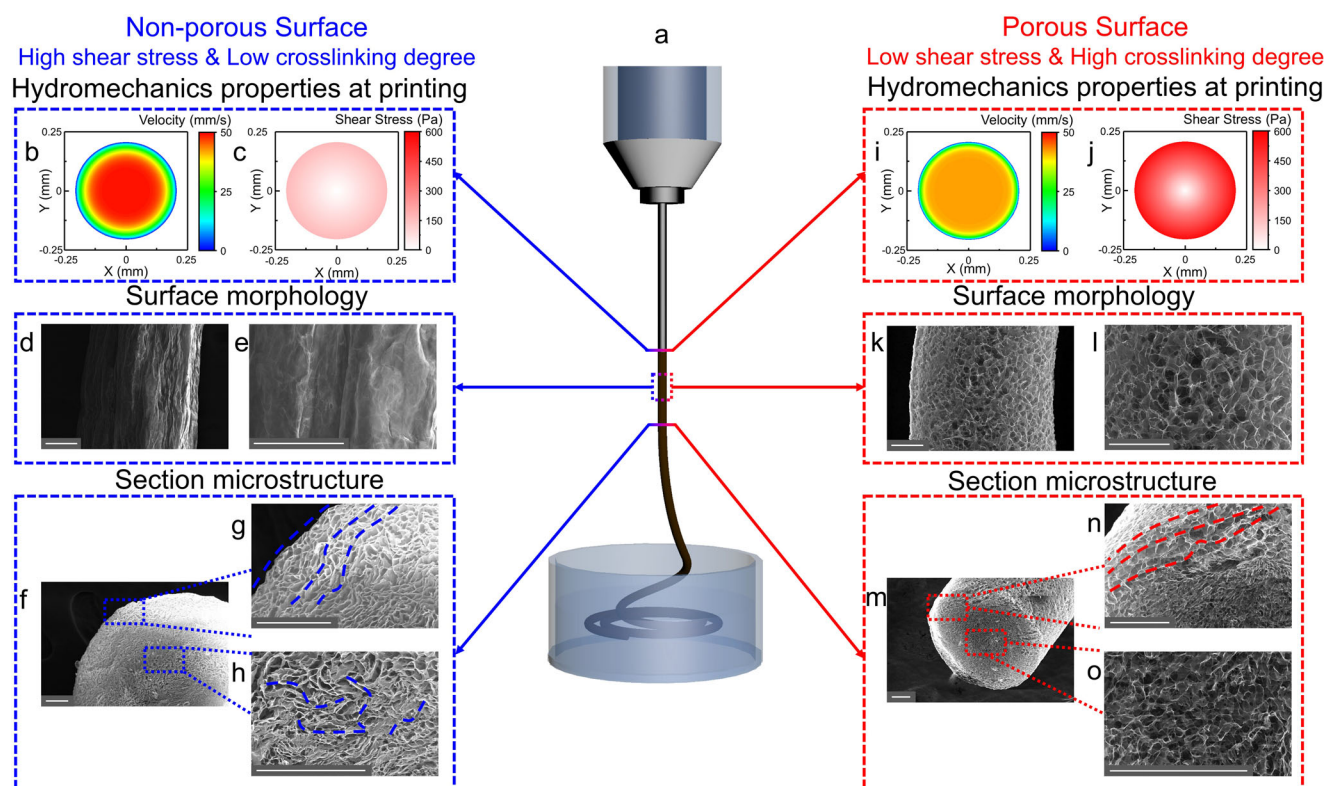


**Fig. 1 Typical non-porous and porous morphology of printed GO aerogel filaments.** **a** Schematic demonstration of directly 3D printing GO ink into liquid nitrogen. **b, c** Distribution of **(b)** velocity and **(c)** shear stress at the nozzle in the printing of pure GO aerogel, printed at 300  $\mu\text{L}/\text{min}$  with nozzle of 0.413 mm. **d, e** Surface SEM figures of as-printed pure GO aerogel. **f–h** Cross-sectional SEM figures of **(f)** section, **(g)** edge of section, and **(h)** centre of section of as-printed pure GO aerogel. **i, j** Distribution of **(i)** velocity and **(j)** shear stress at the nozzle in the printing of aerogel with ascorbic acid (160 mM), printed at 300  $\mu\text{L}/\text{min}$  with nozzle of 0.413 mm. **k, l** Surface SEM figures of as-printed aerogel with 160 mM AA. **m–o** Cross-sectional SEM figures of the **(m)** section, **(n)** edge of section, and **(o)** centre of section of as-printed aerogel with 160 mM AA. Scale bars 100  $\mu\text{m}$ . Distribution of velocity and shear stress are obtained by CFD simulation (see Methods).

We first investigate the correlation between extrusion-induced shear stress and resultant filament microstructure by studying the shear stress distribution and morphology across the cross-section of the extrusion nozzles. Computational fluid dynamics (CFD) simulation with no-slip wall boundary conditions is performed to analyse the hydrodynamic properties in the printing process, including shear stress and velocity distribution (see Methods for details). Due to the resistance from the nozzle wall, the flow velocity at the centre is substantially larger than that close to the edge (see Fig. 1b and Supplementary Fig. 2a). As a consequence, the shear stress also increases from the nozzle centre to the edge (Fig. 1c and Supplementary Fig. 2b). As mentioned above, the relatively high shear stress and corresponding shear flow at the edge of the nozzle are often identified in the literature as the key reason behind the non-porous surface of printed graphene-based aerogels<sup>13,17–19</sup>. We suggest that the non-uniform shear stress due to the velocity gradient forces the randomly distributed GO sheets to align at the inner wall of the nozzle, forming a non-porous aerogel surface fully covered by parallel sheets. The observation of filament microstructure on the sample surface agrees well with our proposal of shear stress alignment (Fig. 1d–h). As shown in Fig. 1d, e, the printed pure GOA demonstrates a typical non-porous surface, fully covered by a wrinkled layer of stacked GO sheets with virtually no observable pore. The GO sheets align well at the edge under relatively high shear stress, forming such structures surrounding the filament (Fig. 1g). Additionally, the cross-section of this non-porous aerogel shows the random alignment of the sheets at the centre to create the porous internal structure due to the low shear stress (Fig. 1f, h). The above observation is in line

with the distribution of shear stress (Fig. 1c) during the extrusion process.

Meanwhile, in a typically porous aerogel with 160 mM AA, printed at the same conditions, the velocity (Fig. 1i and Supplementary Fig. 2b) and shear stress distribution profile (Fig. 1j and Supplementary Fig. 2b) are similar to those of the non-porous aerogel. Hence, a similar cross-sectional microstructure (Fig. 1m–o) is observed. The sheets also tend to partially stack in parallel at the edge but arbitrarily distribute at the centre, consistent with the cross-sectional shear stress distribution. However, in spite of the high absolute value of the shear stress near the nozzle wall, the surface porosity of the resultant aerogel (Fig. 1k, l) is high. We propose that this is due to the high crosslinking degree between the GO sheets induced by the reduction of AA.

The aerogels with 40 mM AA and with 6 mM  $\text{Ca}^{2+}$  printed at different flow rates and nozzle diameters further establish the negative correlation between the surface shear stress and the surface porosity. The addition of 40 mM AA or 6 mM  $\text{Ca}^{2+}$  increases the crosslinking degree of GO ink by reduction and chelation, respectively. Therefore, shear stress becomes the dominant factor for surface porosity in these GO inks with a certain amount of crosslinking additives. As our CFD simulation results show when extruding 25  $\text{mg}/\text{mL}^{-1}$  GO ink with 40 mM AA (Fig. 2a), the shear stress at the edge of the outlet rises along with the increase of flow rate and the narrowing of the nozzle diameter. A clear negative correlation of shear stress and surface porosity is observed in this case (Fig. 2a). With the increase in shear stress, the surface porosity reduces from >40 to <5% for all the combinations of nozzle diameter and flow rate. It is even

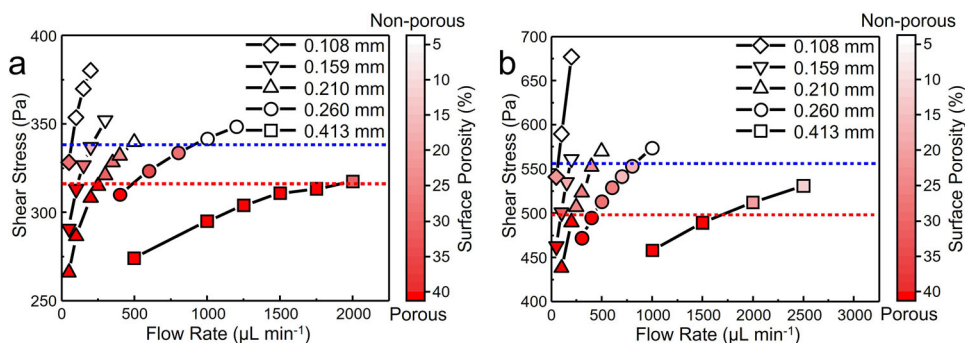


**Fig. 2** The relationship between shear stress and surface porosity. Surface shear stress and surface porosity of aerogels with (a) 40 mM AA and with (b) 6 mM  $\text{Ca}^{2+}$  printed at different flow rates and by nozzles with different diameters. The red and the blue lines mark the shear stress threshold of porous surface and non-porous surface, respectively. Surface shear stress is obtained by CFD simulation (see Methods).

possible to mark two shear stress thresholds for the surface porosity. As shown in Fig. 2a, the aerogels with 40 mM AA printed under shear stress above the blue dotted line ( $\sim 338$  Pa) are all non-porous, while the samples under the red dotted line of  $\sim 316$  Pa are all porous. The filaments printed under the shear stress between these two levels have semi-porous surfaces. A similar trend of surface porosity can be found in the GO ink crosslinked by a certain concentration of calcium ions. Figure 2b shows that the decrease of surface porosity also follows the increase of shear stress in the aerogels with 6 mM  $\text{Ca}^{2+}$ . The shear stress defining the transition between porous and semi-porous surfaces can be labelled at  $\sim 500$  Pa (red line) and that between semi-porous and non-porous at  $\sim 557$  Pa (blue line). Considering the above results, we conclude that the high shear stress in the nozzle during extrusion is directly responsible for the non-porous aerogel surface.

### Crosslinking of GO ink and surface porosity

Apart from the shear stress during printing, we also reveal that the crosslinking degree of GO sheets affects the surface porosity of the resultant aerogels (see Supplementary Fig. 3). Among the reported graphene-based aerogels in Supplementary Table 1, we note that the precursor GO suspensions with crosslinking agents, such as mild reductants<sup>13</sup> or multivalent metal ions<sup>14</sup>, and molecules<sup>22</sup> that can form multiple hydrogen bonds with GO, result in aerogels with a porous surface. Meanwhile, the printing of pure GO suspensions or GO inks with non-crosslinking additives leads to a non-porous surface. To study the influence of crosslinking degree, we use a range of additives commonly used in the literature: AA, calcium ions, and HPMC. Addition of AA to GO suspension partially reduces oxygen-containing groups on the GO sheets, greatly enhancing the  $\pi$ - $\pi$  interaction between them to form the crosslinking network<sup>23,24</sup>. On the other hand, multivalent metal ions such as calcium ions crosslink adjacent GO sheets by coordinating with hydroxyl and carboxyl groups<sup>25</sup>.

Those two representative agents exemplify redox crosslinking dependent on intrinsic  $\pi$ - $\pi$  interaction of reduced GO sheets and non-redox crosslinking relying on supermolecular interaction between the additive molecules and sheets. HPMC, as a comparison, serves solely as a thickener instead of a crosslinker in the GO suspension. Although HPMC forms limited hydrogen bond and van der Waals interaction with GO, it neither reduces the GO sheets nor has strong interactions with them unlike the reductants and the crosslinkers such as AA and  $\text{Ca}^{2+}$ <sup>20</sup>.

In GO inks with increasing AA concentrations, a higher crosslinking degree is revealed through larger apparent viscosities (Fig. 3a). We propose that for a particular ink, the negative correlation between shear stress and surface porosity is valid. For instance, the surface of aerogels with 80 mM AA changes from a porous to a semi-porous state when the CFD-simulated shear

stress increases from 394 to 434 Pa, along with the increase of flow rate. However, for GO inks with different AA concentrations, we suggest that the crosslinking degree replaces the shear stress as the dominant factor in determining surface porosity. Although extruded GO inks of higher crosslinking degree experience higher shear stress due to an increase in viscosity, their surface tends to be more porous under the same extrusion condition (Fig. 3b). Indeed, the aerogels with 160 mM AA samples are always porous, even under very high shear stress when extruded at  $500 \mu\text{L min}^{-1}$ . Additionally, while the aerogels with 80 mM AA transition to a semi-porous surface state at increasingly high flow rates, the filaments with 40 mM AA become semi-porous at  $300 \mu\text{L min}^{-1}$  and show non-porous surface morphology at  $500 \mu\text{L min}^{-1}$ . Meanwhile, pure GO aerogel printed at all flow rates is non-porous, even though it is printed under the lowest shear stress among all the inks.

We also observe that the surface porosity of the aerogel filaments printed by  $\text{Ca}^{2+}$ -crosslinked inks are similar to the above results from the inks modified by AA. As demonstrated in Fig. 3c, GO inks show higher apparent viscosities when  $\text{Ca}^{2+}$  concentration increases from 0 to 7.5 mM, implying a rising crosslinking degree. As before, the aerogels demonstrate a tendency to be more porous with increasing  $\text{Ca}^{2+}$  crosslinker concentration (Fig. 3d) due to high viscosity, even under larger shear stress. Both aerogels with 7 mM  $\text{Ca}^{2+}$  and 7.5 mM  $\text{Ca}^{2+}$  are always porous, while the ones with 2.5 mM  $\text{Ca}^{2+}$  and 5 mM  $\text{Ca}^{2+}$  remain non-porous at all printing flow rates. This is similar to the pure GO sample. As for aerogels with 6 mM  $\text{Ca}^{2+}$ , the printed aerogel filaments demonstrate an obvious porous to semi-porous to non-porous transition with the increase of flow rate from 100 to  $500 \mu\text{L min}^{-1}$ . The enhancement of sheet crosslinking leads to a higher degree of surface porosity, regardless of the types of crosslinking agents used.

Notably, while the addition of HPMC also thickens the GO suspension (Fig. 3e), the surface of both aerogels with 1% HPMC and 2.5% HPMC are always non-porous (Fig. 3f). We propose that without abundant and strong supermolecular interaction, the HPMC additive does not significantly crosslink the GO sheets. This results in low surface porosity of the printed aerogels with HPMC in spite of exhibiting shear stress compared to those of the crosslinkers. We note that other reported non-porous graphene-based aerogels also use non-crosslinked GO inks with various thickeners<sup>5,26,27</sup>. The difference in surface porosity between printed aerogel filaments with AA, calcium ion, and HPMC establishes the relationship between high crosslinking degree and high surface porosity, and excludes high viscosity or other rheological properties as the determining factors.

To conclude, shear stress and the crosslinking degree are two key factors that determine the surface porosity of printed GOA. Among the different types of GO inks, the one with a relatively

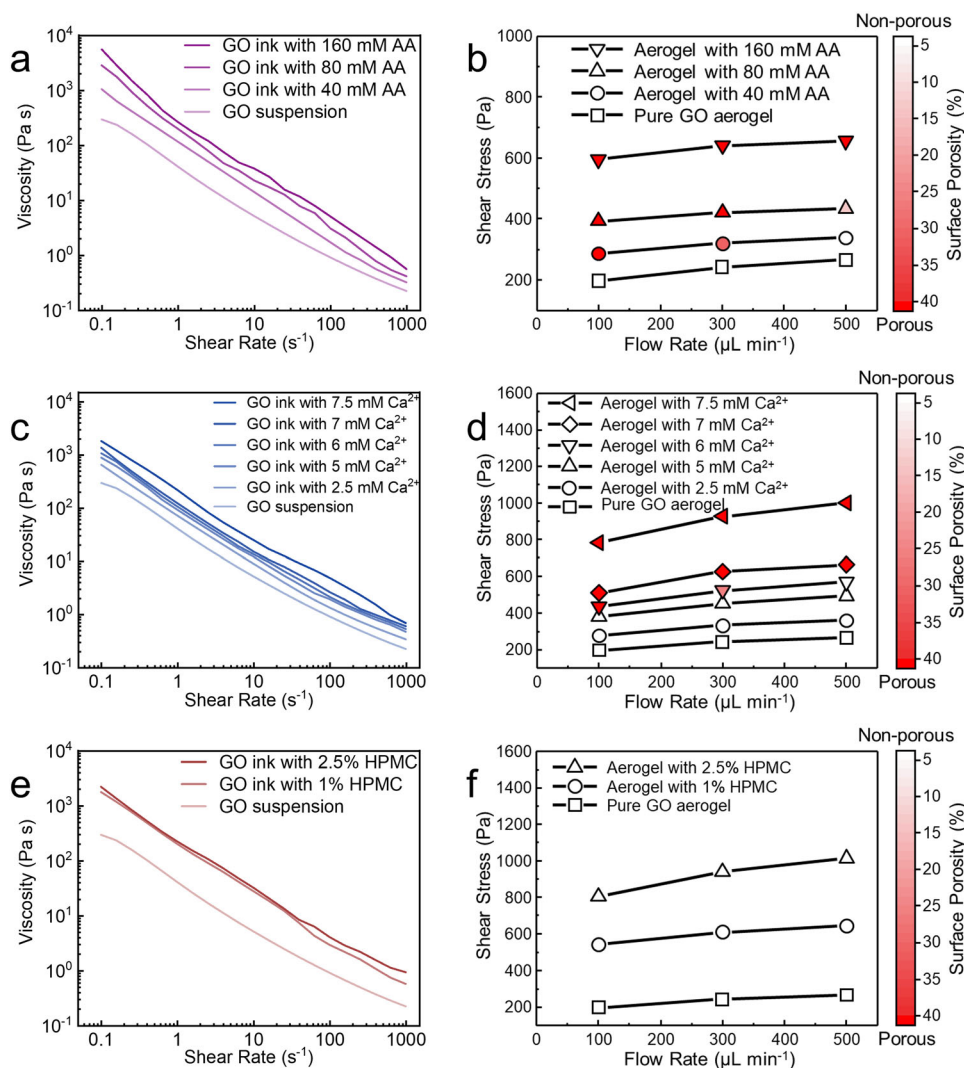


**Fig. 3** The influence of crosslinking degree on surface porosity. **a** Apparent viscosity as a function of shear rate for GO ink modified by AA. **b** Surface shear stress and surface porosity of aerogels with different concentrations of AA, printed by 0.210 mm nozzle. **c** Apparent viscosity as a function of shear rate for GO ink crosslinked by Ca<sup>2+</sup>. **d** Surface shear stress and surface porosity of aerogels with different concentrations of Ca<sup>2+</sup>, printed with 0.210 mm nozzle. **e** Apparent viscosity as a function of shear rate for GO ink mixed with HPMC. **f** Surface shear stress and surface porosity of aerogels with different ratios of HPMC, printed with 0.413 mm nozzle. Surface shear stress is obtained by CFD simulation (see Methods).

high crosslinking degree tends to show a large surface porosity in printed aerogels. In the printing of GO ink with a certain degree of crosslinking, the increase in shear stress gradually reduces the surface porosity. Specifically, for pure GO suspensions or other GO inks of a low crosslinking degree, due to the high shear stress, the GO sheets parallelly align along the inner surface of the nozzle, i.e. the outer surface of the printed structures. Subsequently, during the freeze-drying procedure, the ice crystals grow between the stacked sheets, leading to a non-porous and wrinkled surface. In contrast, the printing of GO inks with appropriate crosslinkers such as mild reductants or multivalent metal ions results in a porous surface, although the sheets still show an alignment trend near the surface of the filament. This can be attributed to the crosslinking of flakes strengthening the self-assembled GO network in suspension<sup>25</sup>. Hence, the interconnected GO network prevents the sheets from being yielded and aligned easily under high shear stress. Thereafter, the ice crystals grow and repel non-directional GO sheets, leaving cellular pores at the surface after sublimation.

Our observation of the effect of crosslinking degree and shear stress on surface porosity is also confirmed in printed monolithic GO aerogels crosslinked by Ca<sup>2+</sup>. The surface porosities of printed monolithic GO aerogels (Supplementary Fig. 4a–f) are similar to those of the corresponding extruded filaments (Supplementary Fig. 4g–l). As shown in Supplementary Fig. 4a–d, g–j, with the Ca<sup>2+</sup> concentration increasing from 0 to 7.5 mM, both the printed and extruded aerogel surface significantly changes from non-porous to porous nature due to the rising crosslinking degree. Additionally, like the extruded samples (Supplementary Fig. 4 i, k, l), the surface porosity also reduces along with the increase of shear stress in the printed monolithic aerogels with 6 mM Ca<sup>2+</sup> (Supplementary Fig. 4c, e, f). Notably, with further increase in the crosslinking degree, high viscosity and inhomogeneous GO aggregation behaviour<sup>25</sup> may significantly affect the ink printability, resulting in nozzle clogging and discontinuous extrusion. However, in our experiments, the crosslinking degree remains relatively low and all the GO inks exhibit excellent homogeneity and printability during the extrusion and printing processes.

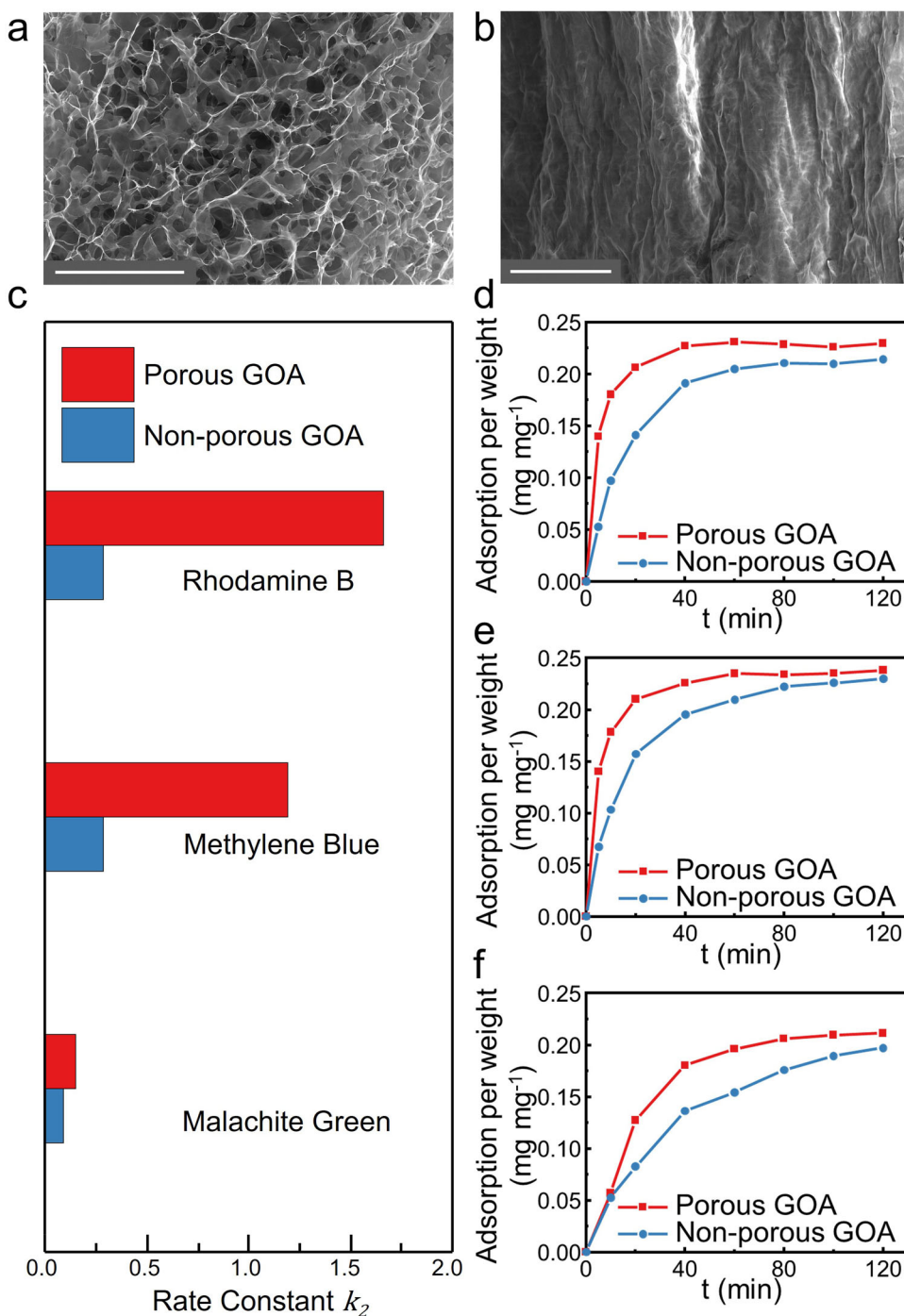


**Fig. 4** Comparison of the structures and dye adsorption performances between porous GOA and non-porous GOA. **a, b** SEM figures of the surface of (a) porous GOA and (b) non-porous GOA. Scale bars 100  $\mu\text{m}$ . **c** Rate constants of adsorption kinetics fitting. **d–f** Dye adsorption curves of porous GOA and non-porous GOA in (d) rhodamine B, (e) methylene blue, and (f) malachite green.

With the principles of surface porosity revealed, it is now possible to control and regulate the surface porosity of printed graphene-based aerogels. For instance, in order to achieve aerogels with a porous surface, a relatively high concentration of crosslinkers can be added to the GO suspension to prepare the ink, since the crosslinking degree has a more significant and determining influence on surface porosity than shear stress. Additionally, in a particular GO ink with an appropriate degree of crosslinking, lowering shear stress by reducing extrusion rate or using a larger nozzle may allow a precise increase in surface porosity.

#### Dye adsorption of porous and non-porous aerogels

We next study the difference in mass transfer efficiency between graphene-based aerogels with porous and non-porous surfaces. We print porous and non-porous aerogels using GO inks cross-linked by 7.5 and 2.5 mM  $\text{Ca}^{2+}$ , respectively and compare their dye adsorption performance. The SEM figures (Fig. 4a, b) demonstrate the distinct surface porosity of these two aerogels, on account of the difference in crosslinking degree.

In dye removal, the diffusion efficiency of absorbed molecules significantly determines the adsorption rate for bulky adsorbents<sup>28</sup>. Therefore, the adsorption efficiency of the porous

graphene-oxide aerogels (GOA) is expected to surpass its non-porous counterpart due to the high surface porosity (see Fig. 4c). Indeed, the GOA with porous surface adsorbs all the tested dyes quicker than the non-porous sample (Fig. 4d–f). Among the models applied to describe the kinetics of the adsorption process<sup>29</sup>, we use the pseudo-second-order model to analyze the porous and non-porous GOA (See Methods) because of the optimal fitting results. As shown in Supplementary Fig. 5, the dye adsorption process of GOA is in line with the kinetic fitting curve based on the pseudo-second-order model, with the  $R^2$  of all the fitting results being  $>0.99$  (Supplementary Table 2). In the adsorption of rhodamine B, the rate constant  $k_2$  of porous and non-porous GOA are 1.663 and 0.282, respectively (Supplementary Table 2). The adsorption rate of porous GOA is  $\times 5.9$  larger than that of the non-porous sample (Fig. 4c). For the case of methylene blue and malachite green solutions, porous GOA also has an advantage, with  $\times 4.2$  and  $\times 1.7$  larger values, respectively.

To ensure that the surface properties of GO do not play a role in the above dye adsorption experiment, we also prepare graphene aerogels (GA) with the porous and non-porous surface by microwave reduction. Compared with GOA, the Raman spectra of GA (Supplementary Fig. 6) shows a sharper  $G$  peak and  $D$  peak, a smaller area ratio of the  $D$  band to  $G$  band ( $A_D/A_G$ ), and a significant  $2D$  peak, indicating the removal of oxygen-containing functional groups and the recovery of intrinsic graphene structure after reduction<sup>30</sup>. Although the dye adsorption of GA is much slower than that of GOA due to the intrinsic hydrophobicity of reduced graphene, the rate difference between porous and non-porous GA still follows the same trend in the adsorption curves (see Supplementary Fig. 7a–c). Applying the pseudo-second-order model to the adsorption process (Supplementary Fig. 7d–f), the resultant rate constants of porous GA are also several times greater than those of the non-porous GA (Supplementary Fig. 8 and Supplementary Table 2). Therefore, the GA with a porous surface also demonstrates a clear advantage over the non-porous counterpart in dye adsorption rates.

Synthesised by the same printing procedure and similar ink recipe, the porous and non-porous aerogels have similar chemical compositions. In addition, specific surface area and inner pore distribution of the GOA or GA with porous and non-porous surfaces are also close to each other (Supplementary Fig. 9). Therefore, we propose that only the surface porosity can be the significant factor that contributes to the adsorption rate difference between these two classes of aerogels. The ability to control and achieve high surface porosity in printed graphene-based aerogels using our strategy here clearly demonstrates its importance for dye adsorption performance.

In conclusion, we demonstrate that the surface porosity of printed graphene-based aerogels can be controlled by shear stress and the degree of crosslinking of the GO sheets in ink. We confirm that the shear stress during extrusion results in a non-porous aerogel surface. In general, the high shear stress aligns the GO sheets, forming a non-porous surface covered with stacked GO sheets. However, a high degree of crosslinking can disrupt this mechanism. In this case, the interconnected and strengthened GO network can resist the shear stress-induced sheet alignment, resulting in a porous surface. Therefore, it is possible to control the surface porosity by regulating the shear stress and crosslinking degree. Simply adding a high concentration of crosslinkers into GO inks could be a reliable method to fabricate porous aerogels. Compared with non-porous counterparts, porous graphene-based aerogels possesses better kinetic performance in dye adsorption, showing a significant advantage in mass transfer efficiency. Our work not only reveals the principles of surface porosity of printed graphene-based aerogels but also provides methods to control the surface porosity. We envisage that our general strategy can be applied to other two-dimensional sheets, towards the design of

their aerogels for applications benefitting from the efficient mass transfer.

## METHODS

### Ink preparation

About 25 mg mL<sup>-1</sup> GO suspension is prepared by mixing GO paste (Sigma-Aldrich) into a certain amount of DI water and magnetically stirring for 4 h.

GO ink with AA is synthesised by adding L-ascorbic acid powder (ACROS Organics) into 25 mg mL<sup>-1</sup> GO suspension and stirring for 15 min by vortex mixer. The mixture is then heated at 60 °C for 1 h. The as-prepared ink is used within 1 day. GO ink with Ca<sup>2+</sup> is synthesised by adding 1 M CaCl<sub>2</sub> solution (Fisher Chemicals) into 25 mg mL<sup>-1</sup> GO suspension and stirring for 15 min by vortex mixer. GO ink with 2.5% or 1% HPMC is prepared by mixing 50 mg mL<sup>-1</sup> GO suspension with equivalent 5 wt% or 2 wt% of HPMC (M.N. 86000, ACROS Organics) in a three-roll mill.

### 3D printing and synthesis

A modified 3D printer (CR-10s, Creality 3D Technology Co.) is used for 3D printing. Briefly, the GO ink is put into a 5-mL-syringe, connected to a female Luer adaptor, PET tube, a modified extruder of the 3D printer, a male Luer adaptor, and the nozzle successively. The syringe is loaded into a syringe pump (ALADDIN-220, WPI Ltd.) to control the extrusion rate of ink.

The GOA filaments are prepared by directly extruding corresponding GO inks into liquid nitrogen. The porous GOA is printed with GO ink with 7.5 mM Ca<sup>2+</sup>, and the non-porous GOA is printed with GO ink with 2.5 mM Ca<sup>2+</sup>. Both are printed at 100  $\mu\text{L min}^{-1}$  with a 0.210 mm nozzle. For all printed samples, a piece of glass wafer is fixed at the printing area as the substrate. After being frozen in liquid nitrogen for 20 min, the samples are freeze-dried overnight by a freeze dryer (LyoQuest, Telstar) to obtain the aerogel filaments or aerogel architecture. Then the aerogels are washed with DI water three to four times to remove excess calcium ions. In the microwave reduction of porous and non-porous GA, the corresponding GOA is heated up to 300 °C for 1 h and microwaved 10 s by 800 W microwave oven, under Ar atmosphere<sup>16</sup>.

### Characterisation

Rheological characteristics of inks are measured by Discovery Hybrid Rheometer HR-1. A disc of 40 mm diameter maintains a measuring gap of 500  $\mu\text{m}$ . The apparent viscosity is recorded with a strain sweep at shear rates from 0.1 to 1000  $\text{s}^{-1}$ . SEM is conducted by FEI Magellan 400 SEM with an acceleration voltage of  $\sim 20$  kV. The GOA samples are sputter-deposited with an Au layer of 5 nm by AGAR AUTO sputter coater before observation to enhance the conductivity. Raman spectra are performed by Renishaw InVia Raman spectrometer with 532 nm laser excitation. Gas sorption analysis is conducted by the NOVA 2200e gas sorption analyzer of ATS Scientific Inc.

### Surface porosity calculation

An optimised MATLAB programme automatically measures the surface porosity of printed filaments<sup>31</sup>. In detail, the input SEM images of the centre of the filaments are first pretreated through background extraction, contrast adjustment, and binarization. The original porous area is then transferred into the hole in the binary image that cannot be reached from the edge of the image. By distinguishing and marking the holes, the surface porosity is obtained by calculating the area ratio of the holes.

### Simulation

ANSYS Fluent software is used to perform CFD numerical simulations of the shear stress and flow velocity distributions during the printing of inks. The flow field inside a nozzle is discretised into 2D-axis-symmetric mesh cells and the macro properties of the fluid cells are computed by solving the incompressible Navier Stokes equations with the no-slip wall boundary condition to set the flow velocity at the wall to be zero. The experimental results concerning the apparent viscosity of the fluids are represented by the non-Newtonian power law. Laminar flow and smooth wall conditions are assumed throughout the simulations. Second-order-accurate numerical schemes are applied. The solution is considered converged when non-dimensional residuals reach  $10^{-7}$ .

## Dye adsorption

Supplementary Table 2 shows the molecular structure of dyes to be absorbed, including rhodamine B (Sigma), methylene blue (Sigma-Aldrich), and malachite green (Sigma-Aldrich). In a typical adsorption experiment, printed GOA or GA is added to 25 ppm dye solution with the volume of 10 mL per mg of adsorbents, then stirred at 200 rpm during the adsorption process at the ambient temperature of 25 °C. The sample solutions are detected by UV-Vis spectrometry at 554 nm for rhodamine B, 664 nm for methylene blue, and 618 nm for malachite green. The pseudo-second-order model is applied for the kinetics of dye adsorption<sup>29</sup>. This model assumes the adsorption rate is linearly proportional to the square of the rest of the adsorption capacity:

$$\frac{dq_t}{dt} = k_2(q_t - q_e)^2 \quad (1)$$

where  $q_t$  is the instantaneous adsorption capacity,  $k_2$  is the rate constant,  $q_e$  is the adsorption capacity at equilibrium.

After integration, the above equation can be transformed to:

$$\frac{t}{q_t} = \frac{t}{q_e} + \frac{1}{k_2 q_e^2} \quad (2)$$

Then, the  $k_2$  and  $q_e$  can be obtained by linear fitting of the above curve.

## DATA AVAILABILITY

All relevant data are available from the corresponding author on request.

## CODE AVAILABILITY

All relevant codes are available at the supporting information or from the corresponding author on request.

Received: 29 December 2021; Accepted: 28 April 2022;

Published online: 24 May 2022

## REFERENCES

- Gorgolis, G. & Galiotis, C. Graphene aerogels: a review. *2D Mater* **4**, 032001 (2017).
- Nassar, G., Daou, E., Najjar, R., Bassil, M. & Habchi, R. A review on the current research on graphene-based aerogels and their applications. *Carbon Trends* **4**, 100065 (2021).
- Feng, J. et al. Printed aerogels: chemistry, processing, and applications. *Chem. Soc. Rev* **50**, 3842–3888 (2021).
- Brown, E. et al. 3D printing of hybrid MoS<sub>2</sub>-graphene aerogels as highly porous electrode materials for sodium ion battery anodes. *Mater. Des* **170**, 107689 (2019).
- Qi, Z. et al. 3D-printed, superelastic polypyrrole-graphene electrodes with ultra-high areal capacitance for electrochemical energy storage. *Adv. Mater. Technol.* **3**, 1800053 (2018).
- Li, L., He, S., Liu, M., Zhang, C. & Chen, W. Three-dimensional mesoporous graphene aerogel-supported SnO<sub>2</sub> nanocrystals for high-performance NO<sub>2</sub> gas sensing at low temperature. *Anal. Chem.* **87**, 1638–1645 (2015).
- Xu, X. et al. Self-sensing, ultralight, and conductive 3D graphene/iron oxide aerogel elastomer deformable in a magnetic field. *ACS Nano* **9**, 3969–3977 (2015).
- Masud, A., Zhou, C. & Aich, N. Emerging investigator series: 3D printed graphene-biopolymer aerogels for water contaminant removal: a proof of concept. *Environ. Sci. Nano* **8**, 399–414 (2021).
- Zhang, Q., Zhang, F., Xu, X., Zhou, C. & Lin, D. Three-dimensional printing hollow polymer template-mediated graphene lattices with tailorable architectures and multifunctional properties. *ACS Nano* **12**, 1096–1106 (2018).
- Wang, Y., Zhang, Y., Wang, S., Guan, Y. & Zhang, Y. A 3D printed synergistic aerogel microreactor toward stable and high-efficiency photocatalytic degradation. *Mater. Today Chem.* **22**, 100566 (2021).
- Sun, M., Chen, C., Chen, L. & Su, B.-L. Hierarchically porous materials: synthesis strategies and emerging applications. *Front. Chem. Sci. Eng.* **10**, 301–347 (2016).
- Wu, L., Li, Y., Fu, Z. & Su, B.-L. Hierarchically structured porous materials: synthesis strategies and applications in energy storage. *Natl. Sci. Rev.* **7**, 1667–1701 (2020).
- Peng, M. et al. 3D printing of ultralight biomimetic hierarchical graphene materials with exceptional stiffness and resilience. *Adv. Mater* **31**, 1902930 (2019).
- Jiang, Y. et al. Direct 3D printing of ultralight graphene oxide aerogel micro-lattices. *Adv. Funct. Mater* **28**, 1707024 (2018).

- Ma, J., Wang, P., Dong, L., Ruan, Y. & Lu, H. Highly conductive, mechanically strong graphene monolith assembled by three-dimensional printing of large graphene oxide. *J. Colloid Interface Sci.* **534**, 12–19 (2019).
- Voiry, D. et al. High-quality graphene via microwave reduction of solution-exfoliated graphene oxide. *Science* **353**, 1413–1416 (2016).
- Huang, K. et al. Anisotropy of graphene scaffolds assembled by three-dimensional printing. *Carbon* **130**, 1–10 (2018).
- Rocha, J. F. et al. Graphene oxide fibers by microfluidics assembly: a strategy for structural and dimensional control. *Nanoscale* **13**, 6752–6758 (2021).
- Zhang, M. et al. Spontaneous alignment of graphene oxide in hydrogel during 3D printing for multistimuli-responsive actuation. *Adv. Sci.* **7**, 1903048 (2020).
- Yao, B. et al. 3D-printed structure boosts the kinetics and intrinsic capacitance of pseudocapacitive graphene aerogels. *Adv. Mater* **32**, 1906652 (2020).
- Tang, X. et al. Architected leaf-inspired Ni<sub>0.33</sub>Co<sub>0.66</sub>S<sub>2</sub>/graphene aerogels via 3D printing for high-performance energy storage. *Adv. Funct. Mater* **28**, 1805057 (2018).
- Tang, X. et al. Generalized 3D printing of graphene-based mixed-dimensional hybrid aerogels. *ACS Nano* **12**, 3502–3511 (2018).
- De Silva, K. K. H., Huang, H.-H. & Yoshimura, M. Progress of reduction of graphene oxide by ascorbic acid. *Appl. Surf. Sci.* **447**, 338–346 (2018).
- Sui, Z., Zhang, X., Lei, Y. & Luo, Y. Easy and green synthesis of reduced graphite oxide-based hydrogels. *Carbon* **49**, 4314–4321 (2011).
- Bai, H., Li, C., Wang, X. & Shi, G. On the gelation of graphene oxide. *J. Phys. Chem. C* **115**, 5545–5551 (2011).
- Zhu, C. et al. Highly compressible 3D periodic graphene aerogel microlattices. *Nat. Commun.* **6**, 6962 (2015).
- Zhu, C. et al. Supercapacitors based on three-dimensional hierarchical graphene aerogels with periodic macropores. *Nano Lett.* **16**, 3448–3456 (2016).
- Yagub, M. T., Sen, T. K., Afroze, S. & Ang, H. M. Dye and its removal from aqueous solution by adsorption: a review. *Adv. Colloid Interface Sci.* **209**, 172–184 (2014).
- Hiew, B. Y. Z. et al. Adsorptive decontamination of diclofenac by three-dimensional graphene-based adsorbent: response surface methodology, adsorption equilibrium, kinetic and thermodynamic studies. *Environ. Res.* **168**, 241–253 (2019).
- Compton, O. C. & Nguyen, S. T. Graphene oxide, highly reduced graphene oxide, and graphene: versatile building blocks for carbon-based materials. *Small* **6**, 711–723 (2010).
- Rabbani, A. & Ayatollahi, S. Comparing three image processing algorithms to estimate the grain-size distribution of porous rocks from binary 2D images and sensitivity analysis of the grain overlapping degree. *Spec. Top. Rev. Porous Media An Int. J.* **6**, 71–89 (2015).

## ACKNOWLEDGEMENTS

This research was supported by EPSRC grant EP/T014601/1. B.Z. would like to acknowledge the CSC-Cambridge scholarship for financial support.

## AUTHOR CONTRIBUTIONS

B.Z. designed and conducted the experiments and analyzed the data. Z.C. performed SEM characterisations. Q.C. and D.L. performed the hydrodynamic simulation. M.X. performed the UV-Vis spectrometry characterisation. G.B. and B.Z. wrote the MATLAB code for calculating surface porosity. B.Z. prepared the manuscript. T.H. supervised the project. All authors analysed and discussed the results and contributed to the final manuscript.

## COMPETING INTERESTS

The authors declare no competing interests.

## ADDITIONAL INFORMATION

**Supplementary information** The online version contains supplementary material available at <https://doi.org/10.1038/s41699-022-00312-w>.

**Correspondence** and requests for materials should be addressed to Tawfique Hasan.

**Reprints and permission information** is available at <http://www.nature.com/reprints>

**Publisher's note** Springer Nature remains neutral with regard to jurisdictional claims in published maps and institutional affiliations.



**Open Access** This article is licensed under a Creative Commons Attribution 4.0 International License, which permits use, sharing, adaptation, distribution and reproduction in any medium or format, as long as you give appropriate credit to the original author(s) and the source, provide a link to the Creative Commons license, and indicate if changes were made. The images or other third party material in this article are included in the article's Creative Commons license, unless indicated otherwise in a credit line to the material. If material is not included in the article's Creative Commons license and your intended use is not permitted by statutory regulation or exceeds the permitted use, you will need to obtain permission directly from the copyright holder. To view a copy of this license, visit <http://creativecommons.org/licenses/by/4.0/>.

© The Author(s) 2022